

Chiral and antichiral edge states in gyromagnetic photonic crystals under magnetic and pseudomagnetic fields

SHIYU LIU,¹ YUTING YANG,^{1,2,*} LIWEI SHI,¹ ENYUAN WANG,³ AND ZHI HONG HANG^{4,5}

¹School of Materials and Physics, China University of Mining and Technology, Xuzhou 221116, China

²State Key Laboratory of Millimeter Waves, Southeast University, Nanjing 210096, China

³School of Safety Engineering, China University of Mining and Technology, Xuzhou 221116, China

⁴School of Physical Science and Technology & Collaborative Innovation Center of Suzhou Nano Science and Technology, Soochow University, Suzhou 215006, China

⁵Institute for Advanced Study, Soochow University, Suzhou 215006, China

*Corresponding author: yangyt@cumt.edu.cn

Received 21 May 2025; revised 20 July 2025; accepted 21 July 2025; posted 21 July 2025 (Doc. ID 568411); published 28 August 2025

Inhomogeneous uniaxial strain-induced lattice deformations result in the Dirac point shift, leading to a strong synthetic pseudomagnetic field. The chiral edge state in the Haldane model and the antichiral edge state in the modified Haldane model can be realized in gyromagnetic photonic crystals, immersed in external real magnetic fields. Here, the interplay of the real- and pseudo-magnetic fields is investigated based on the onsite magnetization modulation and the uniaxial strain within gyromagnetic photonic crystals, thereby resulting in photonic band deformations including the shift of the chiral edge states and the lift of the degenerate antichiral edge states. The experiment is further performed to observe the imbalanced transport of these edge states on two opposite sides. Our findings can help to deeply explore rich and significant physics of synthetic gauge fields, and facilitate designs of photonic functional devices, such as the proposed unidirectional multichannel waveguide. © 2025 Chinese Laser Press

<https://doi.org/10.1364/PRJ.568411>

1. INTRODUCTION

Graphene in a real strong magnetic field can generate discrete Landau levels [1,2]. In recent years, the strain engineering of graphene has become a research field attracting much attention [3–12]. Inhomogeneous uniaxial strain can induce the lattice deformation together with the shift of Dirac points, equivalent to modulating the hopping amplitudes between neighboring lattice sites, thereby giving rise to a synthetic gauge field. Similar to a real magnetic field, it further reveals a strong uniform perpendicular pseudomagnetic field as well as quantized Landau levels, which have been extended to acoustic and photonic crystals [13–31]. Unlike the real magnetic field breaking the time-reversal symmetry, the pseudomagnetic field preserves the time-reversal symmetry with opposite signs at two inequivalent valleys. The distinct nature between the real- and pseudo-magnetic fields can bring interesting phenomena.

In the well-known Haldane model exhibiting the quantum Hall effect, a pair of chiral edge states depending on the topological Chern numbers counterpropagates along two parallel edges [32,33]. Recent studies discovered an intriguing modified Haldane model, resulting in the antichiral edge states copropagating on opposite sides, while the bulk states transport along the opposite direction as required by energy conservation

[34,35]. This modification to the Haldane model can be constructed by reversing the next-nearest-neighbor hoppings at different sublattices, equivalent to reverse magnetic fluxes. These models have been realized in a gyromagnetic photonic crystal (GPC) by onsite modulation of magnetization, with such a structure immersed in an external real magnetic field [36–45]. The competitive relationship between the real- and pseudo-magnetic fields has been studied in graphene [46,47]. However, the transition of the topological edge states under their coexistence is unexplored in the classical wave system.

This work studies the edge state transport in a GPC with the coexistence of real- and pseudo-magnetic fields, as displayed in Fig. 1(a). The chiral edge states emerge in the GPC immersed in the same external real magnetic field, breaking the time-reversal symmetry, on different sublattices. The inhomogeneous uniaxial strain is applied to the GPC to construct an effective gauge field. The combined action of the real- and pseudo-magnetic fields modifies the dispersion curves of the chiral edge states and dispersive Landau levels. Secondly, we simultaneously reverse the magnetization directions of two sublattices and apply the strain, thereby inducing the spatially asymmetric propagation of the antichiral edge states in a GPC. The implemented experiments demonstrate the

deformed edge state dispersions and their imbalanced transport couplings. Based on the modulation of the intensity and direction of the pseudomagnetic fields, we propose a multichannel waveguide, which paves a new way for the further application of photonic devices.

2. CHIRAL EDGE STATE UNDER THE PSEUDOMAGNETIC FIELD

The Haldane model, with broken time-reversal symmetry in the original Dirac-model-based graphene-like honeycomb lattice, is defined by the Hamiltonian [34,42]:

$$H_{\text{Haldane}} = t_1 \sum_{\langle i,j \rangle} c_i^\dagger c_j + t_2 \sum_{\langle\langle i,j \rangle\rangle} e^{-i\nu_{ij}\varphi} c_i^\dagger c_j + \text{H.c.},$$

where t_1 and t_2 are nearest-neighbor hopping and next-nearest-neighbor hopping, respectively. c_i^\dagger and c_j are the creation and annihilation operators at sites i and j . φ represents the hopping phase, and $\nu_{ij} = \pm 1$ indicates the hopping direction at sublattice A or B. The unequal t_2 next-nearest-neighbor hoppings of two sublattices break the time-reversal symmetry, lifting the Dirac degeneracy and opening a completed bandgap. Two edge states counterpropagate along the upper and lower boundaries of the finite structure with the Haldane model. In the continuum theory, the effective Hamiltonian of the Haldane model can be rewritten as [34,48]

$$H = v(\sigma_x \tau_z k_x + \sigma_y \tau_0 k_y) + t_2^a \sigma_z \tau_z + t_2^b \sigma_0 \tau_0,$$

where v is the group velocity around the Dirac point, the Pauli matrices $\sigma_{x,y,z}$ describe the sublattice pseudospin, σ_0 is the 2×2 identity matrix, $\tau_z = +1$ (-1) represents the K (K') valley, and

$k_{x,y}$ is the momentum relative to the Dirac points. In addition, $t_2^a = -3\sqrt{3}t_2 \sin \varphi$ and $t_2^b = -3t_2 \cos \varphi$.

In photonics, the Haldane model can be realized in a GPC under uniform external real magnetic fields B_0 along the z -direction. Figure 1(b) shows the configuration of the GPC with onsite magnetization modulation [41,42]. The gyromagnetic cylinders, arranged in a honeycomb lattice, consist of yttrium iron garnet (YIG) ferrite materials immersed in air. The honeycomb lattice can be divided into two interpenetrating triangular lattices (sublattices A and B). The lattice constant is $a = 10$ mm, the side length is $l_0 = a/\sqrt{3}$, the radius of the YIG cylinder is $r = 1.5$ mm, and the relative permittivity is $\epsilon = 14.5$. Permanent magnets are placed above and below the gyromagnetic cylinders to generate a homogeneous external magnetic field. Both sublattices A and B are subjected to an external real magnetic field, where adjacent sublattices exhibit parallel magnetization bias orientations (as indicated by pink arrows) while maintaining identical magnetic fluxes, as shown in the right panel of Fig. 1(b). This configuration induces strong anisotropy in the YIG cylinders, resulting in a permeability tensor response (see Appendix A for materials characteristics).

We consider an inhomogeneous uniaxial strain applied to a GPC along the y -direction, as shown in Fig. 1(c). The translation invariance is preserved along the x -direction, indicating that the hopping amplitude in the other two directions remains constant. Stretching and compressing the original hexagonal lattice induces the lattice deformation and shifts the degenerate Dirac points along the K-K' direction, as displayed in Fig. 1(d). This is mathematically equivalent to modulating the hopping amplitudes between neighboring lattice sites.

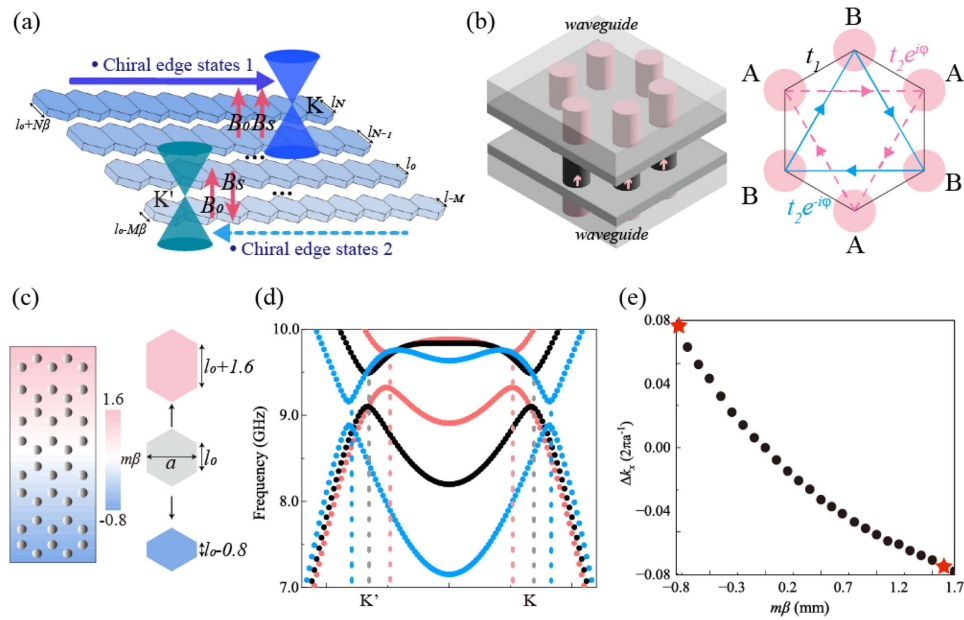


Fig. 1. (a) Schematic of the imbalanced energy transport of the chiral edge states under the coexistence of the real magnetic field B_0 and pseudomagnetic field B_s . (b) Haldane model and GPC configuration. The YIG cylinders are placed in a parallel metallic plate waveguide. Onsite magnetization modulation is realized by placing permanent magnets on the top and bottom of the cylinders. (c) Uniaxially strained GPC structure with a linear lattice deformation along the y axis producing the pseudomagnetic field along the z -direction. The background color indicates the distortion β quantifying the lattice deformation. Right panel: deformation of the honeycomb unit cells under stretching (red) and compression (blue). (d) Shift of the opened Dirac cones along the K-K' direction for the stretched and compressed GPC. (e) Function relationship between lattice deviation $m\beta$ and Dirac point shift denoted by Δk_x .

Here, we introduce a distortion quantity β to quantify the lattice deformation. The displacement of the Dirac points exhibits a linear relationship with $m\beta$ for the m th layer, as illustrated in Fig. 1(e). Consequently, the inhomogeneous strain-induced hopping of the m th stretched and compressed honeycomb layer along the y -direction can be expressed as $l_m = l_0 + (-1)^\alpha m\beta$, where $\alpha = 0$ (1) for stretched (compressed) layers. The hopping amplitudes are set as fixed values: $l_N = l_0 + N\beta$ for the top layer and $l_{-M} = l_0 - M\beta$ for the bottom layer, where M and N denote the number of stretched and compressed layers, respectively. Both the distortion quantity and the associated number of layers can be modulated. In the GPC, the distortion β is modulated as $\beta = (l_N - l_{-M})/(N + M + 1)$. The displacement of Dirac cones gives rise to an effective vector potential $\mathbf{A} = (\delta k_x, 0)$. According to $\mathbf{B} = \nabla \times \mathbf{A}$, the linear variation of $A_x(y)$ induces the emergence of the pseudomagnetic field $B_s = A_x(y)/y$ perpendicular to the x - y plane. The pseudomagnetic fields B_s are oriented along the $+z$ and $-z$ directions at the K and K' valleys, respectively. The number of compressed and stretched layers and the distortion quantity determine the pseudomagnetic field intensity. The effective Hamiltonian at the valleys becomes [46,49]

$$H = v[\sigma_x \tau_z (k_x + A_x) + \sigma_y \tau_0 (k_y + A_y)] + t_2^a \sigma_z \tau_z + t_2^b \sigma_0 \tau_0,$$

where $A_{x,y}$ is the vector potential. Due to the uniform pseudomagnetic field, the energy spectrum in the strained GPC is quantized into discrete Landau levels:

$$E_n = \begin{cases} -\Delta \text{sign}(B_s), & n = 0 \\ \pm \omega_c \sqrt{\Delta^2 + \omega_c^2 n}, & n \neq 0 \end{cases},$$

where n is the Landau level index, the cyclotron frequency is $\omega_c = v\sqrt{2|B_s|}$, and the introduced parameter is $\Delta = t_2^a \tau_z - t_2^b$.

We consider the GPC under the coexistence of the real magnetic field B_0 and pseudomagnetic field B_s . The presence of the B_0 (B_s) breaks (preserves) the time-reversal symmetry in the system. While the real magnetic field is the same for the K and K' valleys, the pseudomagnetic fields exhibit opposite directions for these two valleys. When both B_0 and B_s coexist, the total effective magnetic fields at the two valleys become unbalanced. In the Haldane model, the chiral edge states propagate in opposite directions along two parallel zigzag boundaries. The introduction of the pseudomagnetic field further induces an energy transport imbalance between these two boundaries.

To demonstrate the properties of GPCs under the coexistence of the real- and pseudo- magnetic fields, we conduct an experiment to investigate imbalanced chiral transport. The experimental configuration is shown in Fig. 2(a). The gyromagnetic cylinders, with a radius of $r = 1.5$ mm and height of 5 mm, are precisely positioned between two parallel aluminum plates. A pair of permanent magnets [samarium-cobalt (SmCo)], possessing the same biasing directions, are placed directly above and below the gyromagnetic cylinders to provide a uniform external real magnetic field along the z -direction. Permanent magnets have a radius of 1.5 mm and height of 0.5 mm. To fix their positions, the magnets are embedded in two metallic plates with heights of $h_2 = h_3 = 4$ mm. Two additional metallic plates, with heights of $h_1 = h_4 = 1$ mm,

are placed on the top and bottom to cover the magnets, preventing the microwave leakage in the experimental sample. To probe the internal electric field within the sample, the first and second metallic plates are drilled with 2 mm diameter holes. Due to experimental platform size constraints, the number of layers of the GPC along the y -direction is limited to 7, corresponding to the distortion $\beta = 0.4$ mm. A larger number of layers result in a weaker pseudomagnetic field while fixing the $l_N = l_0 + 1.6$ and $l_{-M} = l_0 - 0.8$. Perfectly electrically conducting boundaries are placed around the gyromagnetic cylinders to confine the edge states, while absorbing materials surround the left and right boundaries to minimize edge scattering. Figure 2(b) shows the top view of the first aluminum plate, featuring two detection channels along the upper and lower boundaries for measurement. Microwave excitation is provided by dipole antennas positioned at the left and right ends of the upper and lower boundaries of the GPC sample.

The dispersion of chiral edge states is experimentally measured and numerically calculated using COMSOL Multiphysics finite element analysis software, as shown in Fig. 2(c). Due to the interplay between the B_0 and B_s , the band dispersion deformation of chiral edge states emerges. The crossing point of two dispersion curves is no longer symmetric about the center of the Brillouin zone and shifts toward the K' valley compared to the $B_s = 0$ case. The group velocities of two chiral edge states are unequal at the K and K' valleys. The upper and lower edges of the sample support right-propagating and left-propagating edge states, respectively. After performing Fourier transforms on the edge E_z electric field mappings, we obtain the edge state dispersions for both the upper and lower boundaries, as shown in the insets of Fig. 2(c). The measured edge state dispersions are in excellent agreement with the simulation results. The varying number of layers in GPCs leads to distinct pseudomagnetic field intensities, which manipulates the edge state dispersion curves, as displayed in Fig. 2(d). The pseudomagnetic field exhibits a significant impact on the upper edge state dispersion compared to that on the lower edge. As the number of structural layers increases, the intensity of the pseudomagnetic field decreases. In the band structure, while the slope direction of the edge state dispersion curves remains unchanged, its magnitude decreases, indicating that the group velocity direction of the upper edge remains constant while its magnitude decreases.

The pseudomagnetic field B_s is larger than the real magnetic field B_0 , causing the signs of the total effective magnetic fields for two valleys (K and K') to be opposite. In our GPC structure, the B_0 is 0.08 T, while the B_s is 1.3 T under the distortion. β is 0.4 mm, corresponding to the number of layers of 7. The coexistence of B_s and B_0 results in deformed edge state dispersions and imbalanced bulk state distributions of Landau levels at the K and K' valleys [45,46]. Furthermore, the chiral edge states do not cross the zeroth Landau level without hybridizing with it. The Landau levels within the bulk bands, induced by strong pseudomagnetic fields, exhibit dispersive rather than flat characteristics. The electric fields of $n = 0, -1$, and -2 Landau levels exhibit distinct spatial distributions for the K' and K valleys in Fig. 2(e), which are attributed to the unequal total effective magnetic fields for two valleys.

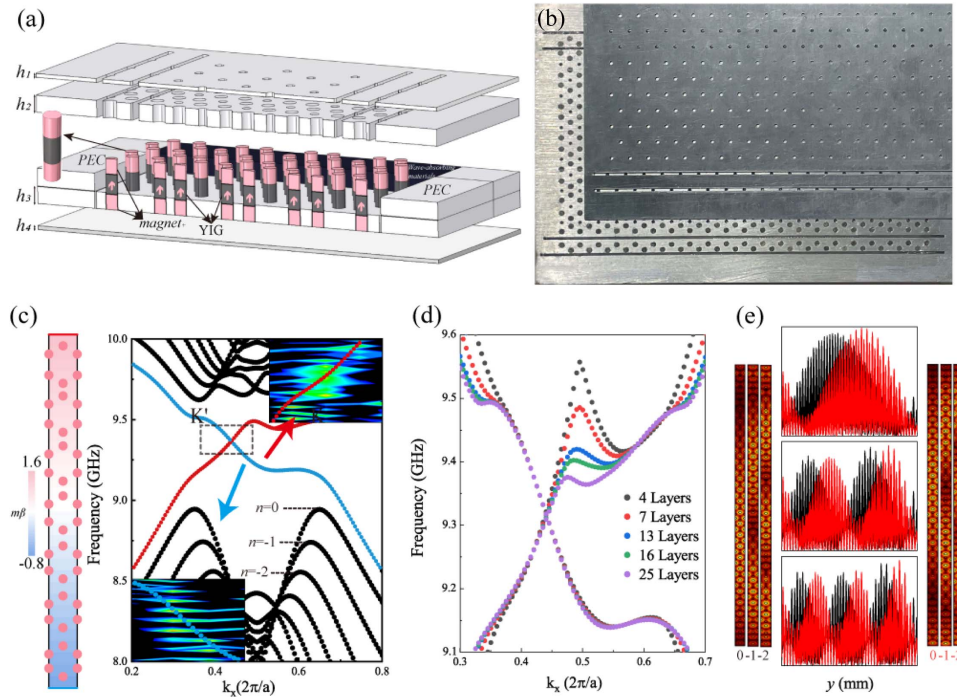


Fig. 2. (a) Schematic diagram of the experimental setup to observe the chiral edge state under the pseudomagnetic field. The gyromagnetic cylinders with a radius of 1.5 mm and height of 5 mm are placed within a waveguide consisting of parallel aluminum plates. Permanent magnets of radius 1.5 mm and height 0.5 mm placed exactly above and below the gyromagnetic cylinders provide a uniform external real magnetic field. (b) Top view of the experimental setup with deformed lattices of 7 layers corresponding to the distortion β of 0.4 mm. (c) Deformed band dispersion of the chiral edge states obtained from numerical simulations and experimental measurements. Upper and lower edge states are denoted by red and blue lines, respectively. (d) Numerically simulated edge state dispersion under different pseudomagnetic field intensities. (e) Left panel: $|E_z|$ eigenfield distributions of the $n = 0, -1$, and -2 Landau levels at the K' valley with the frequencies of 9.08, 9.04, and 9 GHz and $k_x = 0.34(2\pi/a)$. Right panel: eigenfields of the Landau levels at the K valley with the frequencies of 9.08, 9.04, and 9 GHz and $k_x = 0.66(2\pi/a)$. Middle panel: normalized $|E_z|$ as a function of the y coordinate at $n = 0, -1$, and -2 Landau levels.

When the excitation source is positioned at two boundaries of the GPC experimental sample, indicated by two yellow stars in Figs. 3(a) and 3(b), the edge states propagate rightward (leftward) along the upper (lower) edge. The measured electric field distributions, obtained by inserting a probe antenna into the holes within the experimental setup, reveal stronger electric field intensity at the upper edge compared to the lower edge. Subsequently, the probe antennas are placed at P_1 , P_2 , and P_3 points marked by blue stars to measure the transmission coefficients, respectively. The transmission of the chiral edge states is controlled and influenced by the pseudomagnetic field intensity. The pseudomagnetic field leads to an uneven energy distribution of the upper and lower edges during the chiral transmission. This transmission property can be leveraged in the design of photonic devices.

3. ANTICHIRAL EDGE STATE UNDER THE PSEUDOMAGNETIC FIELD

Here, we investigate the interplay between the pseudomagnetic field B_s applied to the modified Haldane model and the real magnetic field B_0 , which results in spatially asymmetric edge state distributions, as shown in Fig. 4(a). The modified Haldane model exhibits antichiral edge states, where two edge states propagate in the same direction while the bulk states

propagate in the opposite direction. The next-nearest-neighbor hopping directions of sublattices A and B are identical, while their hopping phases have opposite signs, as displayed in Fig. 4(b). The Dirac points still remain degenerate, but their energies shift in opposite directions. The most intuitive manifestation in the energy band is the emergence of degenerate edge state dispersions with identical dispersion slopes. The modified Haldane model can be realized in the GPC structure by applying real magnetic fields B_0 in opposite directions to different sublattices. The related parameters of the GPC are the same as those in Fig. 2. The pseudomagnetic field B_s parallel to the $+z$ -direction at the K valley is generated by lattice deformation, similar to that in the original Haldane model. In Fig. 4(c), the pseudomagnetic field leads to the band deformation and lifts two degenerate dispersion curves, with the upper and lower edge state dispersions represented by red and blue lines, respectively. In the experiment configuration, we reverse the biasing directions of adjacent permanent magnets to uniformly apply opposite magnetic fluxes to sublattices A and B. After performing a Fourier transform on the mapped electric fields of the upper and lower edges, we obtain deformed band dispersions that agree well with simulated results. Figure 4(d) shows that the intensity of the pseudomagnetic field B_s significantly influences the upper branch of the antichiral edge state dispersions; its direction of

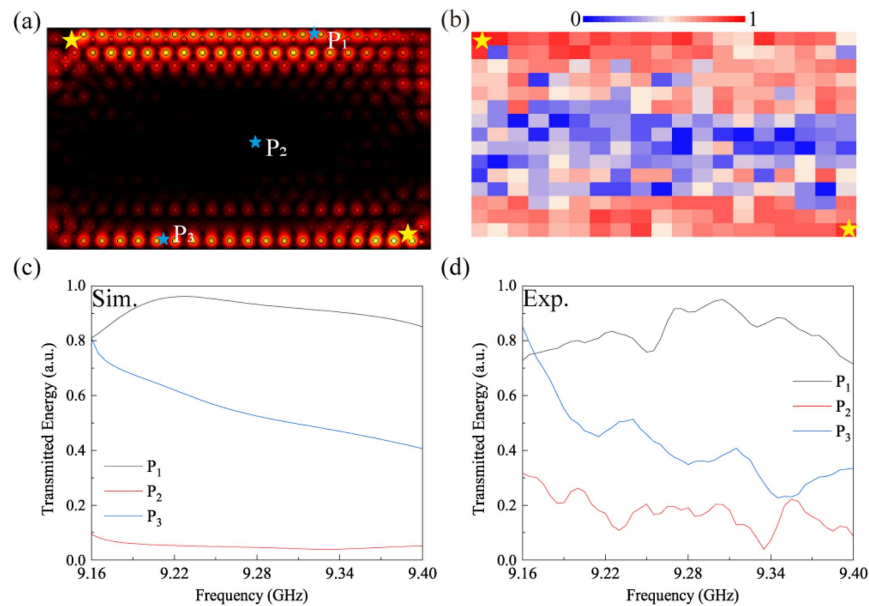


Fig. 3. (a) and (b) Simulated and experimentally measured electric field distribution of the imbalanced edge state transport. The electric field intensity at the upper edge is stronger compared to the lower edge at 9.25 GHz. Yellow stars mark excitation source positions, and blue stars indicate probe locations. (c) and (d) Simulated and measured transmission spectra.

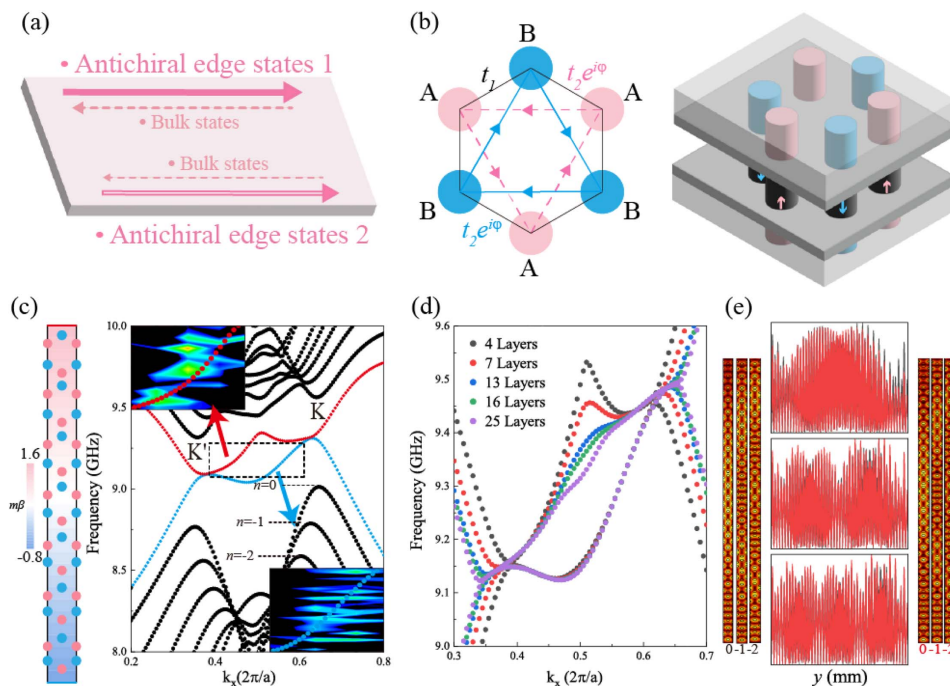


Fig. 4. (a) Spatially asymmetric distribution of the antichiral edge states under the coexistence of the real magnetic field B_0 and the pseudo-magnetic field B_s . (b) Modified Haldane model and GPC configuration. (c) Deformed band structure of the antichiral edge states in numerical simulations and experimental measurements. (d) Band dispersion curves under different B_s intensities. (e) Left panel: $|E_z|$ distributions of the $n = 0, -1$, and -2 Landau levels at the K' valley with the frequencies of 9.01, 8.95, and 8.85 GHz and $k_x = 0.34(2\pi/a)$. Right panel: $|E_z|$ distributions of the Landau levels for the K valley with the frequencies of 9.39, 9.33, and 9.26 GHz and $k_x = 0.66(2\pi/a)$. Middle panel: normalized $|E_z|$ as a function of the y coordinate at $n = 0, -1$, and -2 Landau levels.

the group velocity remains unchanged while its magnitude increases with the enhancement of the pseudomagnetic field intensity.

Figures 5(a) and 5(b) illustrate the transport properties of the antichiral edge state in simulations and experiments. Both the upper and lower edge states propagate toward the right.

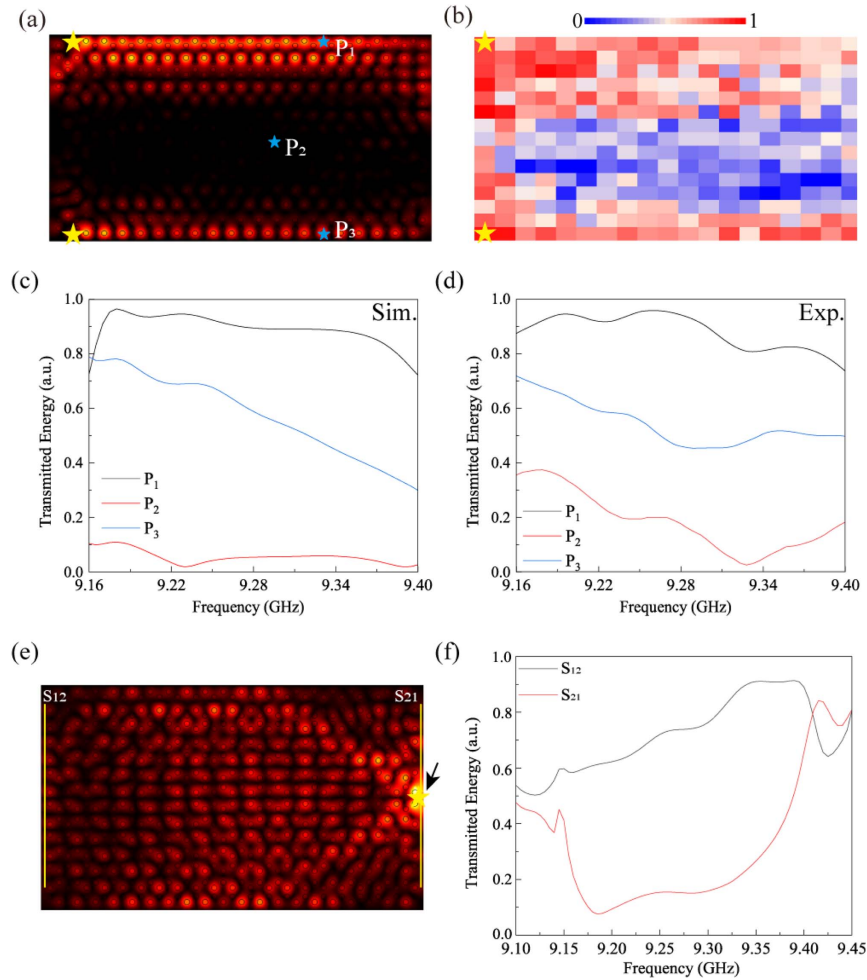


Fig. 5. (a) and (b) Simulated and experimentally measured electric field distribution of the antichiral edge states at 9.18 and 9.2 GHz, respectively. The yellow and blue stars indicate the position of the excited and probed sources, respectively. (c) and (d) Simulated and experimentally measured transmission spectra at P_1 , P_2 , and P_3 . (e) Electric field distribution of the bulk state excited by the excitation source indicated by the black arrow. (f) S_{21} and S_{12} transmission coefficients of the bulk states.

Since the antichiral propagation occurs in a gapless system, the reverse transmission of the bulk states is essential to ensure the energy conservation of the system; thus, there is a weak reverse transmission in the bulk states accompanying the edge state that propagates to the left. The antichiral transmission is controlled by the pseudomagnetic field, which causes the intensity of the upper edge to exceed that of the lower edge. As shown in Figs. 5(c) and 5(d), the transmission at port P_1 within the frequency range of 9.16–9.4 GHz is higher than that at port P_3 . Meanwhile, the transmission at port P_2 always remains at a relatively low level compared to that at ports P_1 and P_3 , indicating that the bulk state transmission is relatively weak. Additionally, the uneven energy distribution of the edge state transmission can be attributed to the presence of the pseudomagnetic field. Figures 5(e) and 5(f) illustrate that, when the excitation source is placed on the left side and incident from the left port, energy transmission in the bulk is prohibited. However, when incident from the right port, it exhibits unidirectional bulk transport, indicating that leftward bulk transport shows strong non-reciprocity.

4. MULTICHANNEL WAVEGUIDE

The energy division on the edges of the GPCs depends on the directions and intensities of the real magnetic field B_0 and pseudomagnetic field B_s . Here, we construct a five-channel unidirectional waveguide based on the characteristic of the counterpropagating chiral edge states and co-propagating antichiral edge states, as shown in Fig. 6(a). We combine two GPCs with opposite B_0 , indicated by red and blue cylinders, to construct a three-channel waveguide with an air gap width of $0.3a$. The inverted uniaxial strain is applied to these two GPCs, resulting in their possession of $+B_s$ and $-B_s$ parallel to the z -direction, indicated by the color map in the inset. Three types of edge state dispersion curves emerge within the GPC bandgap. The group velocities of the chiral edge states on the top and bottom edges are positive, in contrast to the negative group velocity of the chiral edge state in the middle channel, as shown in Fig. 6(c). Therefore, the excited waves propagate toward the right along the top and bottom channels and toward the left along the middle channel. The opposite B_s are also generated in two GPCs with the same modified Haldane modes, as shown

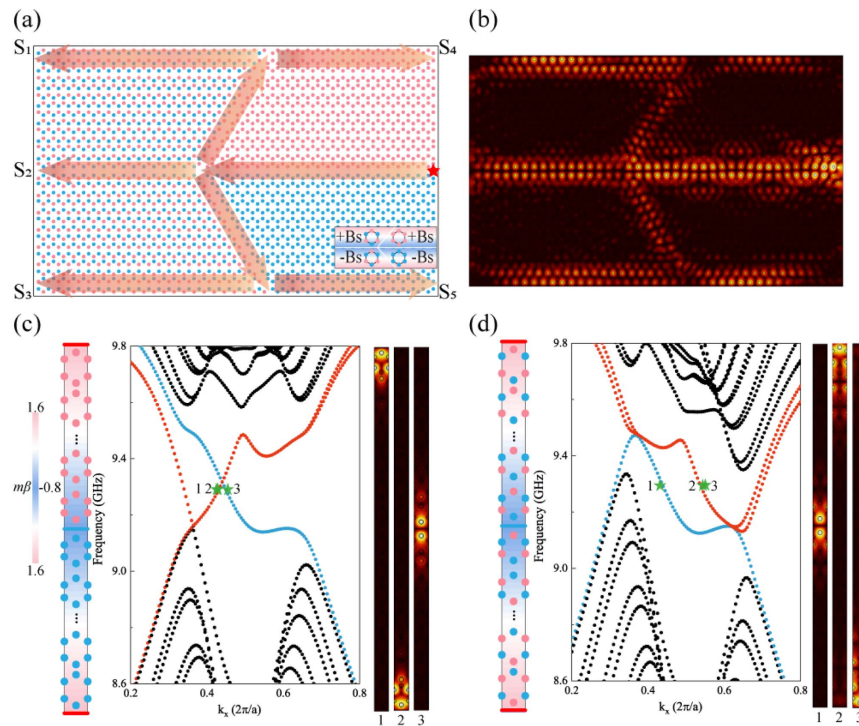


Fig. 6. (a) Schematic diagram of the five-channel unidirectional waveguide composed of four types of GPC structures under the interplay of the real magnetic field B_0 and pseudomagnetic field B_s . The position of the excitation source is marked by a red star, and the transmission channels of electromagnetic waves are marked by red arrows. (b) Simulated electric field distribution of chiral and antichiral edge states at 9.34 GHz. (c) Chiral edge state dispersions of two GPCs with opposite B_s when the number of layers is 7 and the distortion β is 0.4 mm. Right panel: $|E_z|$ eigen-electric field distribution at the frequency 9.24 GHz and the wave vector $k_x = 0.414(2\pi/a)$ and $0.466(2\pi/a)$. Upper and lower edge states are denoted by red lines, and the middle channel is denoted by blue lines. (d) Antichiral edge state dispersions of two GPCs with opposite B_s . Right panel: $|E_z|$ electric fields at the frequency 9.31 GHz and the wave vector $k_x = 0.434(2\pi/a)$ and $0.532(2\pi/a)$.

in Fig. 6(d). The antichiral edge states propagate toward the left along the three channels. The manipulation of B_0 and B_s directions enables control over the energy distributions and transmission directions in different channels, thereby facilitating the design of the beam splitter, as illustrated by the electric field distribution in Fig. 6(b). Since the edge states are strongly confined to the edges and the bulk states are spatially separated from the edge states, they can propagate robustly through a shape 60° angle without backscattering. When we further change B_0 and B_s in the four domains of the beam splitter, the transmission ratio of the five channels can be manipulated (see Appendix C for simulation results), thus allowing additional control over the on-off states of electromagnetic waves at specific output ports. Even though the multichannel waveguide is not experimentally realized owing to the size limit of the experimental platform, the abundant simulated results demonstrate remarkable tunability in the designed multichannel waveguide, therefore providing new methods to design more photonic devices.

5. SUMMARY

By applying the uniaxial strain to GPCs with Haldane model and modified Haldane model, a synthetic pseudomagnetic field parallel to the z -direction can be obtained. The induced pseudomagnetic field does not change the transmission direction of the chiral and antichiral edge states, while leading to an

imbalance in the edge energy distribution. This phenomenon of uneven energy distribution between the upper and lower edges is verified in the measured edge state dispersions and electric fields in the performed experiments. Subsequently, with the joint regulation of the real- and pseudo-magnetic fields, a multichannel electromagnetic wave waveguide is proposed. By manipulating the intensity and direction of the pseudomagnetic field, the transmission energy ratio of each channel can be controlled, which improves the space utilization rate.

APPENDIX A: MATERIAL CHARACTERISTICS

The gyromagnetic material is commercially available yttrium iron garnet (YIG) with a measured relative permittivity 14.5 and a dielectric loss tangent 0.0002. Its measured saturation magnetization is $4\pi M_s = 1800$ G, with a ferromagnetic resonance line width of 20 Oe. Typically, the magnetization will decrease to a negligible value without the presence of the external magnetic field. The relative magnetic permeability of the YIG has the following form:

$$\hat{\mu} = \begin{pmatrix} \mu_r & -i\mu_k & 0 \\ i\mu_k & \mu_r & 0 \\ 0 & 0 & 1 \end{pmatrix},$$

where $\mu_r = 1 + \frac{(\omega_0 + i\alpha\omega)\omega_m}{(\omega_0 + i\alpha\omega)^2 - \omega^2}$, $\mu_k = \frac{\omega\omega_m}{(\omega_0 + i\alpha\omega)^2 - \omega^2}$, with the parameters as $\omega_m = 4\pi\gamma M_s$, $\omega_0 = \gamma B_0$. $\gamma = 1.76 \times 10^{11} \text{ s}^{-1} \text{ T}^{-1}$ is

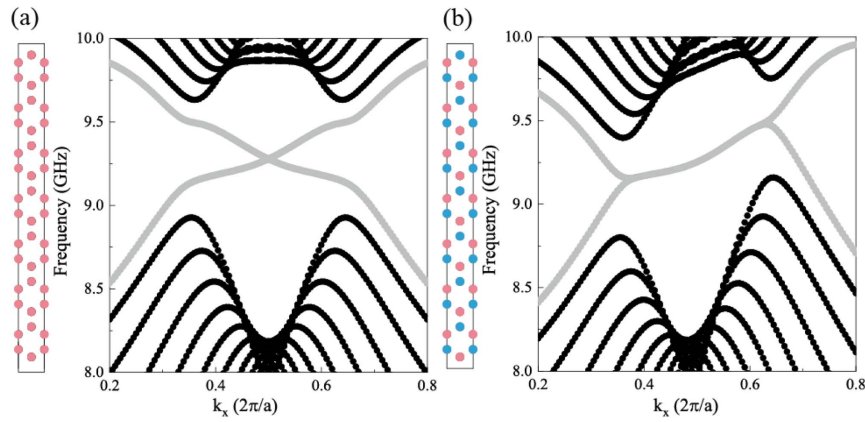


Fig. 7. (a) Schematic of the GPCs with the Haldane model and chiral edge state dispersions within the photonic bandgap. (b) Antichiral edge state in the modified Haldane model.

the gyromagnetic ratio, and ω is the operating frequency. $\mu_r = 0.86$ and $\mu_k = 0.587$. The external magnetic field is $B_0 = 0.08$ T.

APPENDIX B: EDGE STATE DISPERSION OF THE HALDANE MODEL AND THE MODIFIED HALDANE MODEL

Figure 7 illustrates the edge state dispersion curves of the Haldane model and the modified Haldane model.

APPENDIX C: MULTICHANNEL WAVEGUIDE

Figure 8 displays the designed multichannel waveguides with the manipulated transmission ratio. Four domain walls in the GPC structures possess different real magnetic fields B_0 and pseudomagnetic fields B_s . The B_s in four domain walls are parallel and anti-parallel in Figs. 8(a) and 8(c), respectively. Figures 8(b) and 8(d) show the electric field distributions of the multichannel waveguide at 9.22 GHz and 9.23 GHz, corresponding to Figs. 8(a) and 8(c), respectively. The electromagnetic

wave can be controlled and directed to specific output ports. The deformed GPCs have the number of layers of 7, corresponding to the distortion β of 0.4 mm.

Funding. Fundamental Research Funds for the Central Universities (2023ZDYQ11003); National Natural Science Foundation of China (12274315, 52227901); China Postdoctoral Science Foundation (2023M743784); State Key Laboratory of Millimeter Waves (K202407).

Disclosures. The authors have no conflicts to disclose.

Data Availability. The data that support the findings of this study are available from the corresponding author upon reasonable request.

REFERENCES

1. K. V. Klitzing, G. Dorda, and M. Pepper, "New method for high-accuracy determination of the fine-structure constant based on quantized Hall resistance," *Phys. Rev. Lett.* **45**, 494–497 (1980).

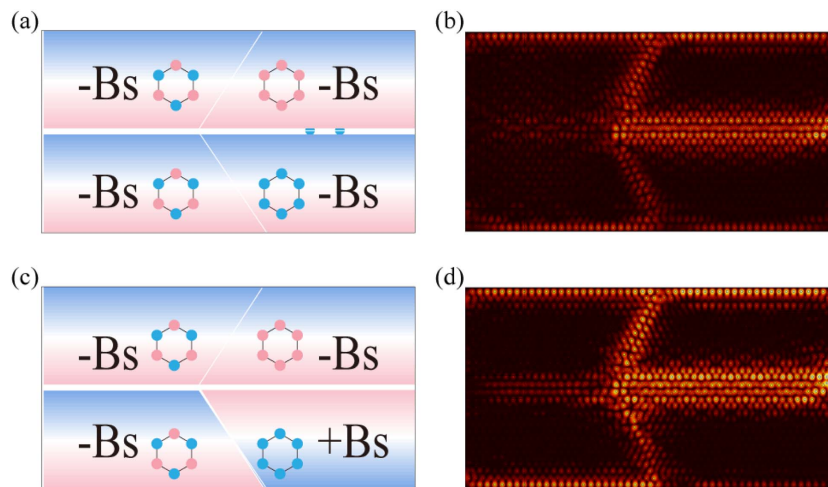


Fig. 8. (a) and (c) Schematic diagram of the five-channel unidirectional waveguide composed of four types of GPC structures under the interplay of the real magnetic field B_0 and pseudomagnetic field B_s . (b) and (d) Electric field distributions at 9.22 GHz and 9.23 GHz corresponding to the structures of (a) and (c), respectively.

2. D. J. Thouless, M. Kohmoto, M. P. Nightingale, *et al.*, "Quantized Hall conductance in a two-dimensional periodic potential," *Phys. Rev. Lett.* **49**, 405–408 (1982).
3. F. Guinea, M. I. Katsnelson, and A. K. Geim, "Energy gaps and a zero-field quantum Hall effect in graphene by strain engineering," *Nat. Phys.* **6**, 30–33 (2010).
4. N. Levy, S. A. Burke, K. L. Meaker, *et al.*, "Strain-induced pseudomagnetic fields greater than 300 Tesla in graphene nanobubbles," *Science* **329**, 544–547 (2010).
5. W. Y. He and L. He, "Coupled spin and pseudomagnetic field in graphene nanoribbons," *Phys. Rev. B* **88**, 085411 (2013).
6. G. Salerno, T. Ozawa, H. M. Price, *et al.*, "How to directly observe Landau levels in driven-dissipative strained honeycomb lattices," *2D Mater.* **2**, 034015 (2015).
7. G. Salerno, T. Ozawa, H. M. Price, *et al.*, "Propagating edge states in strained honeycomb lattices," *Phys. Rev. B* **95**, 245418 (2017).
8. É. Lantagne-Hurtubise, X. X. Zhang, and M. Franz, "Dispersive Landau levels and valley currents in strained graphene nanoribbons," *Phys. Rev. B* **101**, 085423 (2020).
9. B. L. Wu, Z. Q. Zhang, H. Jiang, *et al.*, "Transport property of inhomogeneous strained graphene," *Chin. Phys. B* **30**, 030504 (2021).
10. Z. Q. Bao, J. W. Ding, and J. Qi, "Complex Landau levels and related transport properties in the strained zigzag graphene nanoribbons," *Phys. Rev. B* **107**, 125411 (2023).
11. J. Y. Fang, Y. C. Zhuang, and Q. F. Sun, "Absence of edge states at armchair edges in inhomogeneously strained graphene under a pseudomagnetic field," *Phys. Rev. B* **109**, 045430 (2024).
12. Y. H. Ho, E. V. Castro, and M. A. Cazalilla, "Haldane model under nonuniform strain," *Phys. Rev. B* **96**, 155446 (2017).
13. H. Abbaszadeh, A. Souslov, J. Paulose, *et al.*, "Sonic Landau levels and synthetic gauge fields in mechanical metamaterials," *Phys. Rev. Lett.* **119**, 195502 (2017).
14. C. Rendel, V. Peano, O. J. Painter, *et al.*, "Pseudomagnetic fields for sound at the nanoscale," *Proc. Natl. Acad. Sci. USA* **114**, 3390–3395 (2017).
15. Z. Yang, F. Gao, Y. Yang, *et al.*, "Strain-induced gauge field and Landau levels in acoustic structures," *Phys. Rev. Lett.* **118**, 194301 (2017).
16. X. Wen, C. Qiu, Y. Qi, *et al.*, "Observation of acoustic Landau quantization and quantum-Hall-like edge states," *Nat. Phys.* **15**, 352–356 (2019).
17. J. C. Luo, L. Y. Feng, H. B. Huang, *et al.*, "Pseudomagnetic fields and Landau levels for out-of-plane elastic waves in gradient snowflake-shaped crystals," *Phys. Lett. A* **383**, 125974 (2019).
18. M. Yan, W. Deng, X. Huang, *et al.*, "Pseudomagnetic fields enabled manipulation of on-chip elastic waves," *Phys. Rev. Lett.* **127**, 136401 (2021).
19. M. C. Rechtsman, J. M. Zeuner, A. Tünnermann, *et al.*, "Strain-induced pseudomagnetic field and photonic Landau levels in dielectric structures," *Nat. Photonics* **7**, 153–158 (2013).
20. H. Schomerus and N. Y. Halpern, "Parity anomaly and Landau-level lasing in strained photonic honeycomb lattices," *Phys. Rev. Lett.* **110**, 013903 (2013).
21. O. Jamadi, E. Rozas, G. Salerno, *et al.*, "Direct observation of photonic Landau levels and helical edge states in strained honeycomb lattices," *Light Sci. Appl.* **9**, 144 (2020).
22. M. Bellec, C. Poli, U. Kuhl, *et al.*, "Observation of supersymmetric pseudo-Landau levels in strained microwave graphene," *Light Sci. Appl.* **9**, 146 (2020).
23. C. R. Mann, S. A. R. Horsley, and E. Mariani, "Tunable pseudo-magnetic fields for polaritons in strained metasurfaces," *Nat. Photonics* **14**, 669–674 (2020).
24. J. Guglielmon, M. C. Rechtsman, and M. I. Weinstein, "Landau levels in strained two-dimensional photonic crystals," *Phys. Rev. A* **103**, 013505 (2021).
25. T. Huang, K. B. Hong, R. K. Lee, *et al.*, "Strain-tunable synthetic gauge fields in topological photonic graphene," *Nanophotonics* **11**, 1297–1308 (2022).
26. F. Deng, Y. Sun, X. Wang, *et al.*, "Valley-dependent beams controlled by pseudomagnetic field in distorted photonic graphene," *Opt. Lett.* **40**, 3380–3383 (2015).
27. Z. Qi, H. Sun, G. Hu, *et al.*, "Electrical manipulation of lightwaves in the uniaxially strained photonic honeycomb lattices under a pseudomagnetic field," *Photonics Res.* **11**, 1294–1302 (2023).
28. W. Wang, W. Gao, S. Zhang, *et al.*, "Moiré fringe induced gauge field in photonics," *Phys. Rev. Lett.* **125**, 203901 (2020).
29. B. Yang, X. Shen, L. Shi, *et al.*, "Nonuniform pseudo-magnetic fields in photonic crystals," *Adv. Photonics Nexus* **3**, 026011 (2024).
30. M. Barsukova, F. Grisé, Z. Zhang, *et al.*, "Direct observation of Landau levels in silicon photonic crystals," *Nat. Photonics* **18**, 580–585 (2024).
31. S. Liu, Y. Yang, M. Li, *et al.*, "Coupled pseudo-magnetic field and valley spin in photonic crystals," *APL Photonics* **10**, 036112 (2025).
32. F. D. M. Haldane, "Model for a quantum Hall effect without Landau levels: condensed-matter realization of the 'parity anomaly'," *Phys. Rev. Lett.* **61**, 2015–2018 (1988).
33. J. Ningyuan, C. Owens, A. Sommer, *et al.*, "Time- and site-resolved dynamics in a topological circuit," *Phys. Rev. X* **5**, 021031 (2015).
34. E. Colomés and M. Franz, "Antichiral edge states in a modified Haldane nanoribbon," *Phys. Rev. Lett.* **120**, 086603 (2018).
35. Y. T. Yang, D. J. Zhu, Z.-H. Hang, *et al.*, "Observation of antichiral edge states in a circuit lattice," *Sci. China Phys. Mech. Astron.* **64**, 257011 (2021).
36. S. Raghu and F. D. M. Haldane, "Analogues of quantum-Hall-effect edge states in photonic crystals," *Phys. Rev. A* **78**, 033834 (2008).
37. Z. Wang, Y. Chong, J. D. Joannopoulos, *et al.*, "Observation of unidirectional backscattering-immune topological electromagnetic states," *Nature* **461**, 772–775 (2009).
38. Y. Poo, R. X. Wu, Z. Lin, *et al.*, "Experimental realization of self-guiding unidirectional electromagnetic edge states," *Phys. Rev. Lett.* **106**, 093903 (2011).
39. G. G. Liu, P. Zhou, Y. Yang, *et al.*, "Observation of an unpaired photonic Dirac point," *Nat. Commun.* **11**, 1873 (2020).
40. J. Chen, W. Liang, and Z. Y. Li, "Antichiral one-way edge states in a gyromagnetic photonic crystal," *Phys. Rev. B* **101**, 214102 (2020).
41. P. Zhou, G. G. Liu, and Y. Yang, "Observation of photonic antichiral edge states," *Phys. Rev. Lett.* **125**, 263603 (2020).
42. J. Chen and Z. Y. Li, "Prediction and observation of robust one-way bulk states in a gyromagnetic photonic crystal," *Phys. Rev. Lett.* **128**, 257401 (2022).
43. X. Xi, B. Yan, L. Yang, *et al.*, "Topological antichiral surface states in a magnetic Weyl photonic crystal," *Nat. Commun.* **14**, 1991 (2023).
44. Y. C. Zhou, H. S. Lai, J. L. Xie, *et al.*, "Magnetic corner states in a two-dimensional gyromagnetic photonic crystal," *Phys. Rev. B* **107**, 014105 (2023).
45. Y. C. Zhou, Z. Q. Sun, H. S. Lai, *et al.*, "Observation of photonic Chern metal with bi-chiral edge propagation," *Laser Photonics Rev.* **18**, 2400826 (2024).
46. Y. C. Zhuang and Q. F. Sun, "Phase diagrams and edge-state transitions in graphene with spin-orbit coupling and magnetic and pseudomagnetic fields," *Phys. Rev. B* **106**, 165417 (2022).
47. M. Manna and S. Haddad, "Strain tuned topology in the Haldane and the modified Haldane models," *J. Phys. Condens. Matter* **32**, 225501 (2020).
48. J. E. Yang, X. L. Lü, and H. Xie, "Modulation of antichiral edge states in zigzag honeycomb nanoribbons by side potentials," *Commun. Phys.* **6**, 62 (2023).
49. P. Li, J. D. Sau, and I. Appelbaum, "Robust zero-energy bound states in a helical lattice," *Phys. Rev. B* **96**, 115446 (2017).